Report for the Joint Use/Research of the Institute for Planetary Materials, Okayama University for FY~~2024~~
2023

14/03/2024

Category: ☑International Joint Research ☐General Joint Research ☐Joint Use of Facility
☐Workshop

Name of the research project: Iron carbide-water reaction under mantle conditions

Principal applicant: Keng-Hsien Chao

Affiliated institution and department: University of Hawaii at Manoa

Collaborator

Name: Takashi Yoshino

Affiliated institution and department: Highly-Advanced Compression of Terrestrial Objects

Research report:

Our visit to IPM was 31/01/2024-02/03/2024. In our visit, we intended to experimentally investigate the iron carbide-water reaction in the pressure and temperature conditions of mantle with the 5000-ton Kawai-type multi-anvil press. We have conducted seven runs of successful multi-anvil press experiments, as well as finished the analysis with Raman spectrometer and EPMA during our visit. The data supports our argument and is of good quality for publication. We are currently working on the manuscript to publish our results from IPM. The specific content of this project and summary are below.

Introduction

H, C, O, N, and S are crucial volatiles on Earth, serving as the building blocks of life, greenhouse gases, and potentially important light elements in the core or powering the dynamo (Hirose et al., 2021). The specific sources, abundance, and distribution of Earth's volatiles remain active topics of debate and research (Dalou et al., 2017; Dasgupta et al., 2013; Grewal et al., 2019; Hirschmann, 2006; Marty, 2012; Shi et al., 2022; Wang and Becker, 2013).

The traditional models proposed that carbon is a siderophile element and would have joined the core during the early history of core formation (Dasgupta et al., 2013; Fischer et al., 2020). Consequently, the carbon concentration in the mantle should be as minor as ~1-5 ppm (Dasgupta et al., 2013). These models generally explain the relatively low carbon concentration in Bulk Silicate Earth as well as the density deficiency in the core. However, the specific carbon concentration in

the mantle is still greater than the prediction of such models, ~120 ppm in pyrolite (McDonough and Sun, 1995). The specific reason for such a surprisingly high carbon concentration in the mantle remains controversial (Dasgupta et al., 2013).

The most well-known hypothesis to explain the unexpectedly high carbon concentration in the mantle is that the volatile-rich late veneers might have delivered additional carbon to the silicate portion of Earth after core formation and the solidification of the mantle completed (Wänke, 1981). However, the isotope feature of carbon in the average mantle is largely different from that of CI chondrite (Deines, 2002; Kerridge, 1985); the H/C ratio of the bulk silicate Earth being greater than that of CI chondrite also contradicts this hypothesis (Hirschmann and Dasgupta, 2009).

A recent study by Ko et al. (2022) proposed the iron carbide-water reaction at the core-mantle boundary releases carbon into Bulk Silicate Earth to be an alternative explanation of the high carbon concentration in the mantle. Assuming the core is made of Fe_3C, resulting from the Fe-C alloy droplets drained into the core in Earth's early history, the diamond forms when the water from the subduction slabs encounters and reacts with the core. The diamond is then recycled back to the mantle, contributing to the modern carbon concentration in Bulk Silicate Earth. However, Ko et al. (2022) only investigated the iron carbide-water reaction at the pressure and temperature (*P-T*) conditions relevant to the core-mantle boundary without data below 70 GPa.

Meanwhile, it is believed that metallic iron (Fe^0) exists in the modern mantle below 250 km due to the $3\ Fe^{2+} = Fe^0 + 2\ Fe^{3+}$ disproportionation reaction (Armstrong et al., 2019; Bindi et al., 2020; Frost et al., 2004; Rohrbach et al., 2011; Rohrbach and Schmidt, 2011). When the metallic iron encounters a carbon-bearing species (e.g., carbonate or carbon hydrides), typically from organic sources on the subduction slabs, Fe_3C or Fe_7C_3 iron carbide forms (Kaminsky, 2012; Lai et al., 2022), although Ko et al. (2022)'s study is restricted to the pressure and temperature condition of the core-mantle boundary, it inspired us with new ideas on this topic: could an iron carbide-water reaction occur in the mantle, where the *P-T* conditions is much lower than the core-mantle boundary?

Research Purpose

In this study, we intend to answer the question of whether the iron carbide-water reaction can cause elemental carbon (C^0) at a *P-T* condition much lower than the core-mantle boundary. If elemental carbon, in diamond or amorphous carbon, forms at such a lower *P-T* condition, two questions can be solved.

1. If water did exist in the early magma ocean, the iron-carbon alloy droplets would react with water and release elemental carbon left behind in the magma ocean on their way,

sinking to the core. Such a mechanism would be able to explain the ~120 ppm of carbon concentration in the silicate portion of Earth.

2. It is confirmed that iron carbide exists in the modern mantle. If the iron carbide scattering in the mantle can encounter water and produce diamonds, it provides a new mechanism of diamond formation and would become a new factor that needs to be considered to study the deep carbon cycle.

Research Conducted

We used the 5000-ton Kawai-type multi-anvil device in the Insititute for Planetary Material, Okayama University, Japan. Fe_3C and Fe_7C_3 were packed with $Mg(OH)_2$ into two separated Pt capsules. These two capsules with different compositions were then loaded into the same Cr, Co-doped semi-sintered octahedral MgO pressure transmitting medium with each side in 14 mm. The specific assembly is in Fig. 1.
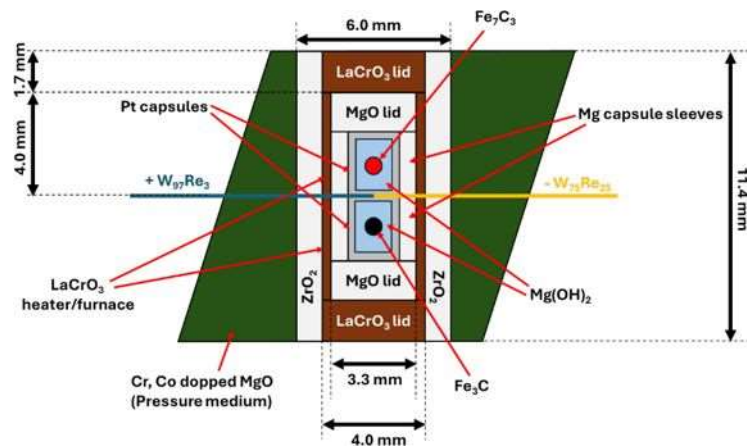

Figure 1. Specific cell assembly for 5000-ton Kawai-type MAP experiments. Cr, Co dropped MgO and ZrO_2 were chosen as pressure transmitting medium and thermal insulator, respectively. $W_{97}Re_3$ and $W_{75}Re_{25}$ alloy wires are inserted and hooked at the center of cell to serve as thermal couple. Two Pt capsules with $Fe_3C+Mg(OH)_2$ and $Fe_7C_3+Mg(OH)_2$ are loaded above and below the thermal couple. The capsule was then sealed by MgO sleeves and lid, followed by $LaCrO_3$, which served as both heater and furnace.

All experiments have identical dimensions of cell assembly as Fig.1 but different truncations of WC cubes depending on the target pressure. The Fe_3C-$Mg(OH)_2$ sample and Fe_7C_3-$Mg(OH)_2$ sample were compressed to 15 GPa with 8 mm truncated WC cubes and compressed to 23 GPa with 5 mm truncated WC cubes, respectively. After reaching the target pressure, the sample was first

heated to 500°C at a heating rate of approximately 100°C/minute; then, it was heated from 500°C to the target temperature, 1000-1600°C, at a heating rate of 700°C/minute. Samples were kept at the maximum temperature for approximately 1-10 minutes. The heating duration at maximum temperature was generally shorter at higher temperatures, as the reaction occurred faster when the temperature rose. Specific pressure and temperature conditions are summarized in Table 1. Meanwhile, Fe_7C_3 was revealed to be more reactive and may disappear rapidly under high temperatures based on the preliminary result of a pilot study at the University of Hawaii. Therefore, to preserve the reaction texture with unreacted iron carbide grain, both the Fe3C-Mg(OH)2 sample and Fe7C3-Mg(OH)2 were kept at the maximum temperature for the identical duration, and the heating duration was no more than 10 minutes to prevent unreacted Fe_7C_3 completely disappears. Specific pressure and temperature conditions, as well as the capsules used, are summarized in Table 1.

Table 1. Summary of pressure, temperature, heating duration, and cell setup in 5000-ton Kawai-type MAP experiments.

Run No.[a]	P (GPa)[b]	T (°C)[b]	Maximum T duration (min)	Cell assembly
0214	15	1000	10	Fe_3C + $Mg(OH)_2$ in Pt capsule; Fe_7C_3 + $Mg(OH)_2$ in Pt capsule
0209	15	1200	7.5	Fe_3C + $Mg(OH)_2$ in Pt capsule; Fe_7C_3 + $Mg(OH)_2$ in Pt capsule
0218	15	1400	3	Fe_3C + $Mg(OH)_2$ in Pt capsule; Fe_7C_3 + $Mg(OH)_2$ in Pt capsule
0208	23	1000	10	Fe_3C + $Mg(OH)_2$ in Pt capsule; Fe_7C_3 + $Mg(OH)_2$ in Pt capsule
0202	23	1200	5	Fe_3C + $Mg(OH)_2$ in Pt capsule; Fe_7C_3 + $Mg(OH)_2$ in Pt capsule
0204	23	1400	5	Fe_3C + $Mg(OH)_2$ in Pt capsule; Fe_7C_3 + $Mg(OH)_2$ in Pt capsule
0206	23	1600	1	Fe_3C + $Mg(OH)_2$ in Pt capsule; Fe_7C_3 + $Mg(OH)_2$ in Pt capsule

[a] Run number is named with the real order of experiments conducted but not listed in the order of temperature in this table.

[b] Table is listed from low pressure to high pressure. Then low temperature to high temperature.

[c] Heating duration reduces with temperature increases, given that reaction speed rises with temperature.

Sample capsules from completed experiments were embedded in epoxy and polished until the center of the capsule was exposed. After the samples were polished, we probed the area surrounding the unreacted iron carbide grain with Raman spectrometer to determine the evidence of carbon-rich materials or diamonds. Data collection was conducted with under total power of 50 mW. Collection time was typically 1-60 seconds, with 3-10 times of spectrum stacked, depending on the signal quality and signal strength of peaks.

After detecting diamond or amorphous carbon near iron carbide grain in the retrieved sample with Raman spectrum, to more specifically characterize the carbon distribution and concentration in the sample, the sample was then coated with gold. Chemical compositions, elemental mapping, and images were determined using the field emission electron microprobe JEOL JXA-IHP200F in IPM. The element mapping was conducted with an acceleration voltage of 15 keV, a current of 100 nA, and a spot size of up to 1 μm. The mapping was done with a pixel area of 1 μm $\times$ 1 μm, 20 milliseconds per pixel. The carbon element map was then converted into semi-quantified carbon concentration using the calibration curve and ZAF methods. The calibration curve method was applied to characterize the carbon concentration of unreacted iron carbide (where the carbon concentration is lower than 10 wt%) with 15 keV, 100 nA, 1 μm $\times$ 1 μm - 3 μm $\times$ 3 μm beam. In contrast, the ZAF method was applied to characterize the carbon-rich area. A 15 keV, 10 nA, focused beam was aimed at where confirmed to be diamond or amorphous carbon in the Raman spectrum. The C element map was converted to a specific carbon concentration map with the X-ray intensity of iron carbide grains and diamond or amorphous carbon grains.

Research outcome

Here, we report the representative results of Fe_3C-$Mg(OH)_2$ reactions and Fe_7C_3-$Mg(OH)_2$ reactions under 23 GPa, 1000°C and 1200°C. The elemental mapping reveals C-rich rims appear in both Fe_3C-$Mg(OH)_2$ reaction (Fig. 2) and Fe_7C_3-$Mg(OH)_2$ reaction (Fig. 3). We probed the Raman spectrum of seven locations and six locations on the C-rich rims of the retrieved sample of Fe_3C-$Mg(OH)_2$ reactions under 23 GPa, 1000°C (Fig. 2c) and Fe_7C_3-$Mg(OH)_2$ reactions under 23 GPa, 1000°C (Fig. 3c), respectively. In contrast to diamond with a single peak at ~1332 cm^{-1}, the Raman spectrum of both Fig. 2 and Fig. 3 show two broad peaks with maximum intensity located at wavenumber approximately 1350 cm^{-1} and 1580 cm^{-1}, respectively. These two peaks are the D-band and G-band of amorphous carbon (Dychalska et al., 2015; Knight and White, 1989; Prawer and Nemanich, 2004), suggesting the C-rich rims are indeed non-crystalline carbon rather than diamond. This is mainly because of the lower temperature at 1000°C, making the crystallization of carbon slow; thus, diamonds cannot form within the short experiment time. Despite the fact that the carbon is not crystalline, the elemental mapping and Raman spectrum are still robust evidence

supporting the argument of elemental carbon forms through Fe_3C-H_2O or $Fe_7C_3-H_2O$ reaction under such *P-T* condition: the Fe is oxidized into FeO and forms (Mg,Fe)O solid solution, while the carbon is expelled by the iron carbide and forms the C-rich rims surrounding the unreacted Fe_3C or Fe_7C_3 grains.
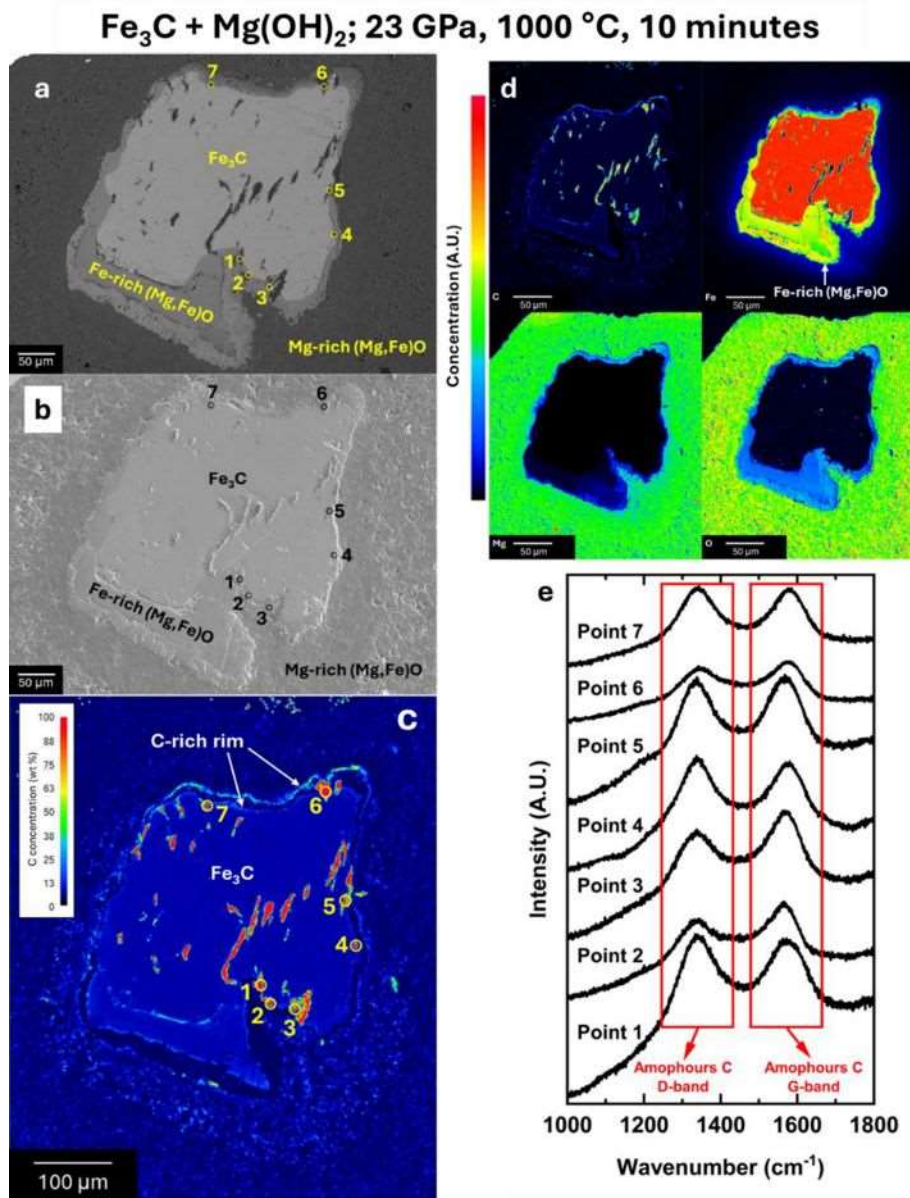

Figure 2. Amorphous carbon formation via $Fe_3C-Mg(OH)_2$ reaction at 23 GPa, 1000°C. Backscattered electron image (a) and secondary electron image (b) of exposed fresh Fe_3C. The calibration curve quantified C concentration map (c) and elemental mapping reveal a C-rich rim surrounding the unreacted iron carbide. The Fe is oxidized into FeO and then mixed with MgO to form (Mg,Fe)O. Raman spectrum (e) containing D-band and G-band supports that the carbon is in amorphous form on the six probed locations on the C-rich rim labeled on (a)-(c).
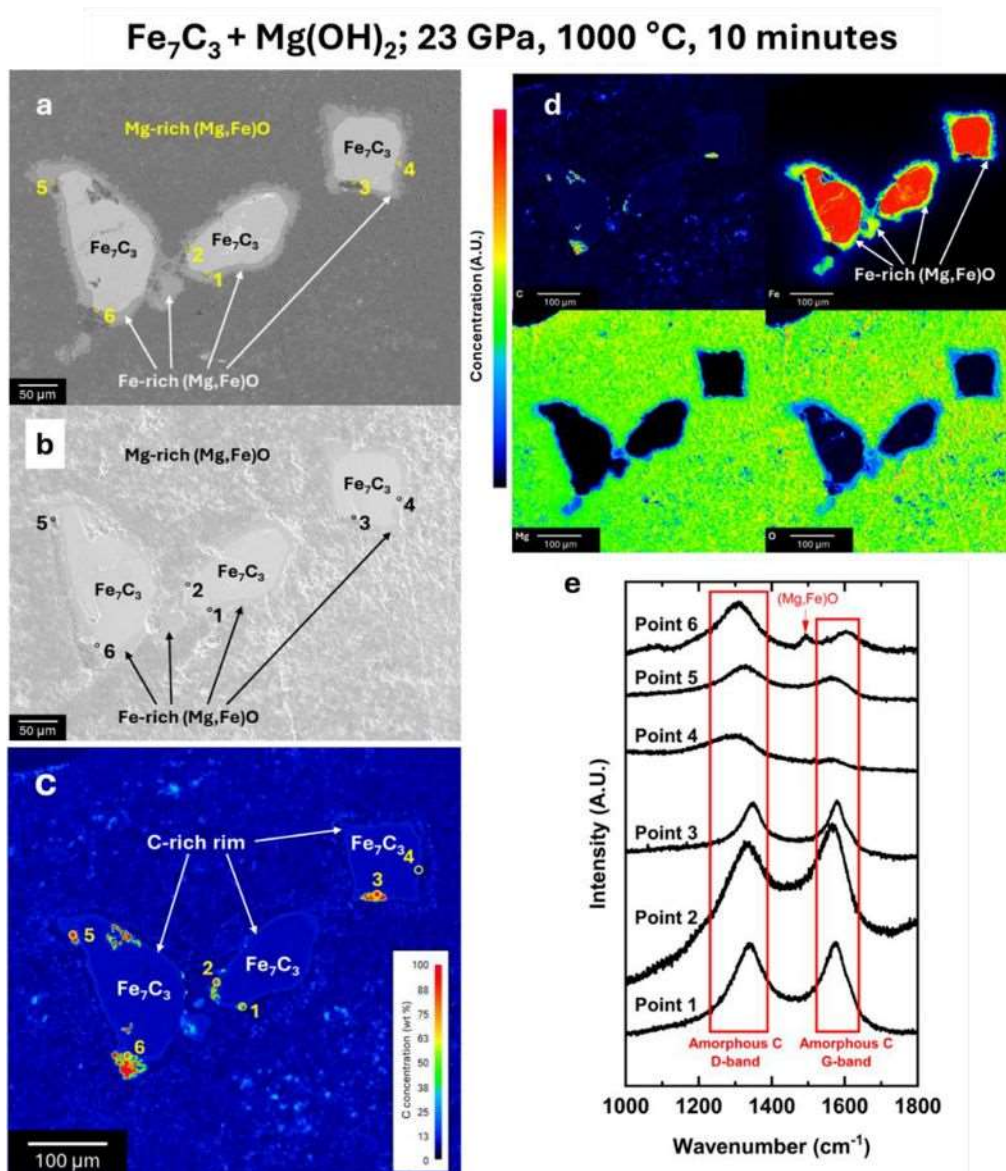
Figure 3. Amorphous carbon formation via Fe_7C_3-$Mg(OH)_2$ reaction at 23 GPa, 1000°C. Backscattered electron image (a) and secondary electron image (b) of exposed fresh Fe_3C. The calibration curve quantified C concentration map (c) and elemental mapping reveal a C-rich rim surrounding the unreacted iron-carbon. The Fe is oxidized into FeO and then mixed with MgO to form (Mg,Fe)O. Raman spectrum (e) containing D-band and G-band supports that the carbon is in amorphous form on the six probed locations on the C-rich rim labeled on (a)-(c).

In those runs of Fe_3C-$Mg(OH)_2$ reactions under 23 GPa, 1200°C (Fig. 4) and Fe_7C_3-$Mg(OH)_2$ reactions under 23 GPa, 1200°C (Fig. 5), we probe 5-6 locations with a Raman spectrometer on the C-rich rim. The spectrum with a single and sharp peak demonstrates that the C-rich rim is composed of crystalline diamond rather than amorphous carbon. This is because a higher temperature at 1200°C favors the speed of diamond crystallization more than that of experiments at

1000°C. Interestingly, the diamond confirmed with the Raman spectrum has a wavenumber range from 1324-1329 cm^{-1} (Fig. 4 and Fig. 5). The carbon-rich area is a polycrystalline diamond, and the Raman peak position and signal strength of the diamond typically decreases with individual crystal size. The diamond's characteristic wavenumber of Raman peak, 1332 cm^{-1}, is equivalent to ~7.5 μm when converted to wavelength. If the average grain size of individual diamonds is in a similar order of ~7.5 μm or smaller, the photon with wavenumber ~1332 cm^{-1} is scattered by diamond grains and less likely to be detected by the spectrometer. Consequently, the peak position of the Raman signal of the diamond decreases to ~1324 cm^{-1} (Namba et al., 1992). In addition to the grain size, if the diamond is not a perfect crystal, the disorder of the sp^3 bond of carbon also contributes to the decrease of wavenumber (Knight and White, 1989; Prawer and Nemanich, 2004).

Although both experiments have diamond formation confirmed, interestingly, the diamond formed in the Fe_7C_3-$Mg(OH)_2$ reactions experiment under 23 GPa, 1200°C (Fig. 5) has a sharper Raman peak than that of Fe_3C-$Mg(OH)_2$ reactions experiment under 23 GPa, 1200°C (Fig. 4), suggesting the diamond formed via Fe_7C_3-$Mg(OH)_2$ reaction is better crystalized than that of Fe_3C-$Mg(OH)_2$ reactions. The higher reactivity of Fe_7C_3 may contribute to the better crystalline diamond than that of the Fe_3C-$Mg(OH)_2$ reaction under identical P-T conditions and heating duration. Another evidence is that the C-rich rim of Fe_7C_3-$Mg(OH)_2$ reactions experiment under 23 GPa, 1200°C (Fig. 5a, Fig. 5c, and Fig. 4.5d) is thicker than that of Fe_3C-$Mg(OH)_2$ reactions experiment under 23 GPa, 1200°C (Fig. 4a, Fig. 4c, and Fig. 4d). Indeed, the C-rich rim of Fig. 4a is thinner than 1 μm, and we had difficulty collecting the Raman signal through the whole C-rich rim of Fig. 4, making the Raman spectrum data restricted to the local area. However, we still found five data with diamonds located on the C-rich rim of Fig. 4a. Therefore, our argument that carbon is expelled from the iron carbide after it reacts with water is still supported, even if the C-rich rim is thin or not well crystallized.
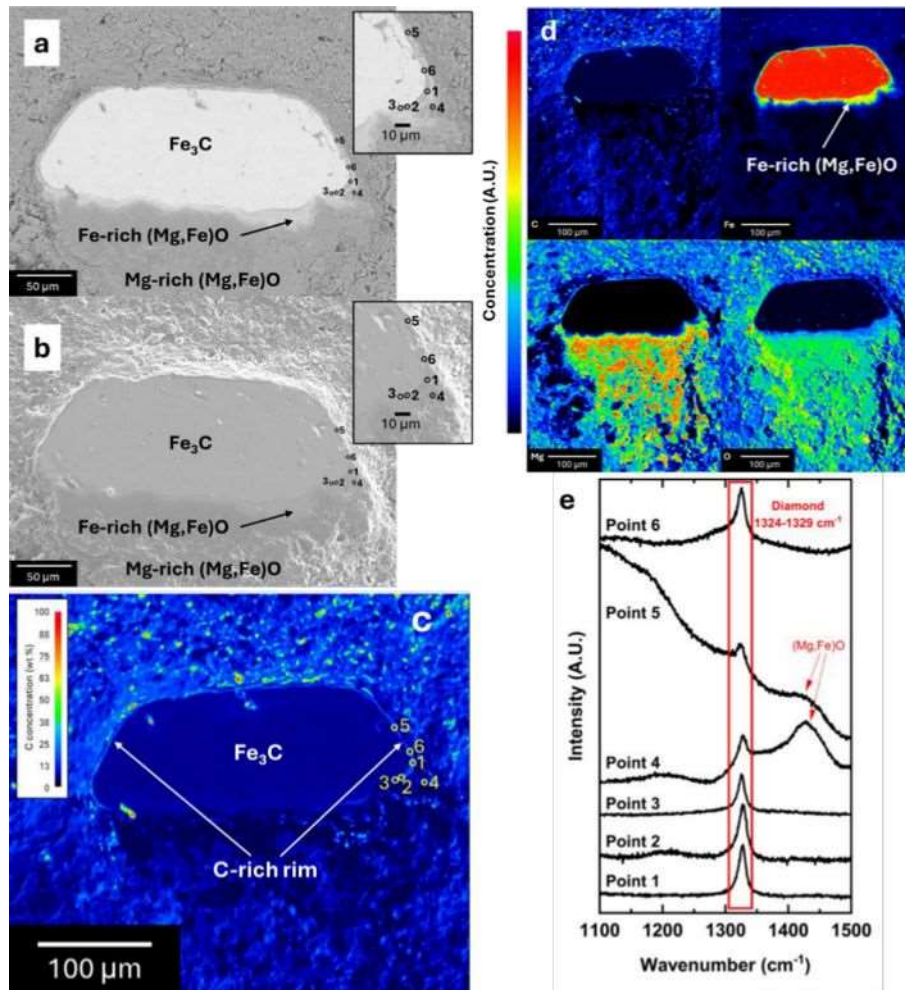
Figure 4. Diamond formation via Fe$_3$C-Mg(OH)$_2$ reaction at 23 GPa, 1200°C. Backscattered electron image (a) and secondary electron image (b) of exposed fresh Fe$_3$C. The calibration curve quantified C concentration map (c) and elemental mapping reveal a C-rich rim surrounding the unreacted iron carbide. Fe is oxidized into FeO; and then mixed with MgO to form (Mg,Fe)O. Raman spectrum (e) shows a diamond peak at wavenumber = 1324-1329 cm^{-1}, providing direct evidence confirming the formation of the diamonds at five locations of (a)-(c).
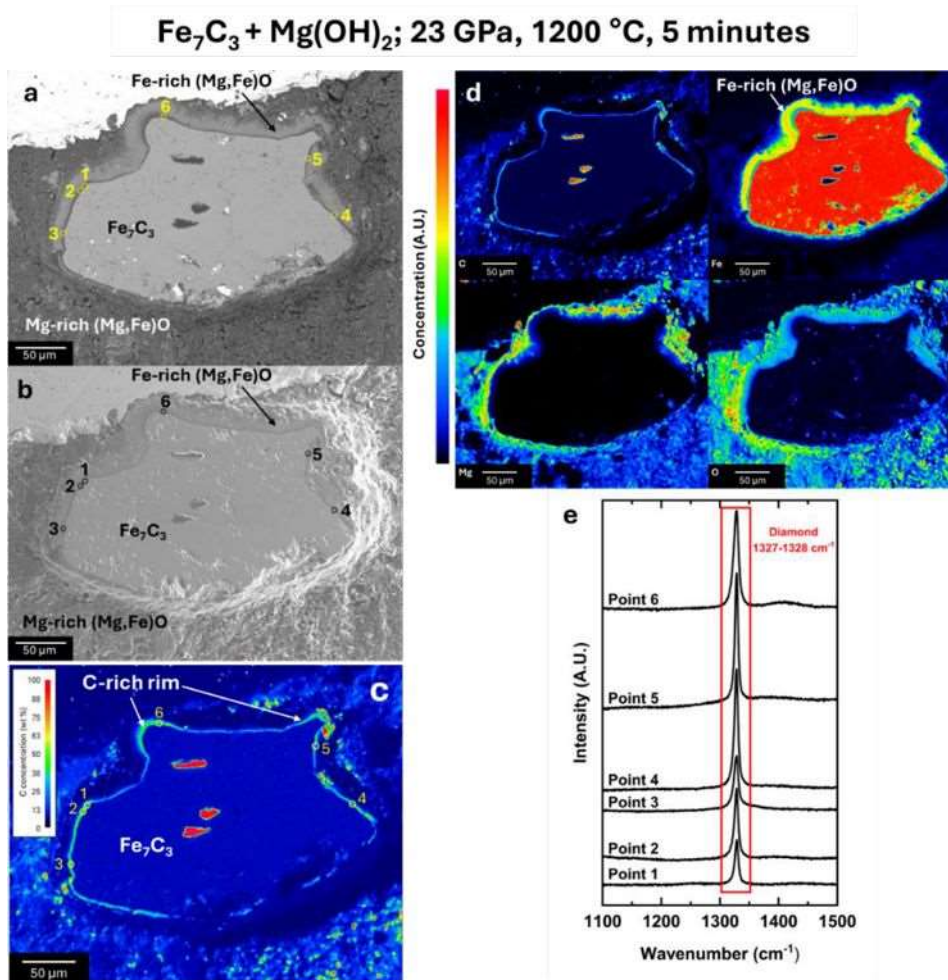
Figure 5. Diamond formation via Fe$_7$C$_3$-Mg(OH)$_2$ reaction at 23 GPa, 1200°C. Backscattered electron image (a) and secondary electron image (b) of exposed fresh Fe$_7$C$_3$. Calibration curve quantified C concentration map (c) and elemental mapping reveal a C-rich rim surrounding the unreacted iron carbon. Fe is oxidized into FeO; and then mixed with MgO to form (Mg,Fe)O. Raman spectrum (e) shows diamond peaks at wavenumber = 1327-1328 cm^{-1}, providing direct evidence confirming the formation of diamond at five locations of (a)-(c). Meanwhile, the Raman peak of the diamond in this data set is sharper and better crystalline than that of Fig. 4.9. The elemental mapping also shows a thicker C-rich rim than that of Fig. 4.9. These two features suggest that the Fe$_7$C$_3$ is more reactive than Fe$_3$C and favors the production of diamond.

In summary, we have done 12 successful experiments covering 15-23 GPa, 1000-1600°C. The chemical species identified, along with the corresponding experimental conditions, are summarized in Table 2. All runs of experiments have the elemental carbon (C^0), in the form of either diamond or amorphous carbon, as well as (Mg,Fe)O identified as the reaction products. The specific mechanism of elemental carbon formation through the chemical reaction can be described as the equations below:

$$Mg(OH)_2 = MgO + H_2O \qquad (1)$$

$$Fe_3C + 3\ H_2O = 1\ C^0 + 3\ FeO + 3\ H_2 \qquad (2)$$

$$Fe_7C_3 + 7\ H_2O = 3\ C^0 + 7\ FeO + 7\ H_2 \qquad (3)$$

$$n\ FeO + 1\text{-}n\ MgO = (Mg_n,Fe_{1\text{-}n})O \qquad (4)$$

First, in equation (1), $Mg(OH)_2$ decomposes into MgO and H_2O as a water source at approximately 900°C or above (Guo et al., 2022). Subsequently, Fe_3C/Fe_7C_3 reacts with H_2O to form diamond, FeO, and H_2 (equation (2) and (3)). The H_2 rapidly diffuses and leaves the system upon formation. It is important to note that the multi-anvil press is an open system, and the H_2 cannot be sealed or retrieved. The FeO is then expelled from the fresh iron carbide grain and combines with MgO to form a (Mg,Fe)O solid solution in equation (5). As FeO diffuses from the fresh iron carbide to the surroundings, the Mg/Fe ratio exhibits spatial dependence, with higher Fe concentration in areas closer to fresh iron carbide and Mg concentration showing the opposite trend.

Table 2. Summary of experimental conditions and species in sample chamber identified through Raman spectroscopy or electron microprobe after reaction of MAP experiments.

Run No.[a]	Starting iron carbide	Pressure (GPa)[b]	Maximum T (°C)[b]	Capsule material	Maximum T duration (min)	Species identified
0214-1	Fe_3C	15	1000	Pt	10	Fe_3C, (Mg,Fe)O, Amorphous C
0209-1	Fe_3C	15	1200	Pt	7.5	Fe_3C, (Mg,Fe)O, Dia, Amorphous C
0218-1	Fe_3C	15	1400	Pt	3	Fe_3C, (Mg,Fe)O, Dia
0208-1	Fe_3C	23	1000	Pt	10	Fe_3C, (Mg,Fe)O, Amorphous C
0202-1	Fe_3C	23	1200	Pt	5	Fe_3C, (Mg,Fe)O, Dia
0204-1[f]	Fe_3C	23	1400	Pt	5	Fe_3C, (Mg,Fe)O, Dia
0214-2	Fe_7C_3	15	1000	Pt	10	Fe_7C_3, (Mg,Fe)O, Amorphous C
0209-2	Fe_7C_3	15	1200	Pt	7.5	Fe_7C_3, (Mg,Fe)O, Dia, Lonsdaleite[e]
0218-2	Fe_7C_3	15	1400	Pt	3	Fe_7C_3, (Mg,Fe)O, Dia
0208-2	Fe_7C_3	23	1000	Pt	10	Fe_7C_3, (Mg,Fe)O, Amorphous C
0202-2	Fe_7C_3	23	1200	Pt	5	Fe_7C_3, (Mg,Fe)O, Dia
0206-2[g]	Fe_7C_3	23	1600	Pt	1	(Mg,Fe)O, Dia[e]

[a] Run No. are based on the real order of experiment rather than the order of pressure or

temperature. For Kawai-type experiments, Fe_3C and Fe_7C_3 are loaded into the sample cell. The "-1" and "-2" stand for Fe_3C and Fe_7C_3 in Table 4.2, respectively.

[b] The table is listed in the order of Fe_3C then Fe_7C_3; low pressure to high pressure; then low temperature to high temperature.

[c] Walker-type MAP Experiments are conducted at University of Hawaii. The experiments typically take 30-40 minutes to reach maximum temperature.

[d] Kawai-type MAP Experiments are conducted at the Institute for Planetary Materials, Okayama University. The experiments typically take 5-10 minutes to reach maximum temperature.

[e] Fe_7C_3 fully reacted and disappeared after the experiments.

[f] Fe_7C_3 counterpart was lost during sample polishing.

[g] Fe_3C counterpart was lost during sample polishing.

Geophysical implications

We have investigated the Fe_3C-H_2O reaction and Fe_7C_3-H_2O reaction using a multi-anvil press at 15-23 GPa with 12 successful runs in IPM. The *P-T* conditions in this study cover the top and bottom of the mantle transition zone. All experiments with various temperature conditions in this study demonstrate the formation of elemental carbon under 15-23 GPa. Since diamonds are stable above 5 GPa (Glosli and Ree, 1999), we have sufficient reason to believe that diamonds could probably form via the iron carbide-water reaction at any pressures between 23-130 GPa (lower mantle to core mantle boundary) if the oxygen fugacity favors reduced carbon species. Based on our experimental results, we propose two possible scenarios concerning the iron carbide-water reaction.

Firstly, during the metal separation period in Earth's early history, Fe-C alloy droplets were stirred by convection and scattered in the magma ocean (Rubie et al., 2015; Wood et al., 2006). The metal droplets eventually reached the core due to their higher density but would have been stirred by convection and suspended in the magma ocean for a period of time. Although the early magma ocean was traditionally believed to be dry due to the minor water content and reduced chemical composition of accretion material (Albarède, 2009), recent studies argue that the magma ocean could have gained water when the hydrogen-rich early atmosphere reacted with silicate melt (Young et al., 2023). Assuming there was a considerable amount of water dissolved in the early magma, the Fe-C alloy droplets might have reacted with water and turned into diamonds under *P-T* conditions significantly lower than those at the core-mantle boundary (~130 GPa) (Fig. 6). In Fig. 6, we illustrate the iron carbide droplets drifting in the magma ocean encounter water and turn into diamond. The diamond was then left behind in the magma ocean, contributing to the ~120 ppm of carbon inventory (McDonough and Sun, 1995) in the Bulk Silicate Earth after the magma ocean solidified. Such a scenario could explain the higher carbon concentration in the mantle without

subduction slabs delivering water to the core, much earlier than the onset of plate tectonics, from the early Hadean to 700 Ma (Hawkesworth et al., 2020). It is still possible that some carbon in the modern carbon inventory of Bulk Silicate Earth is released from the Fe_3C-water reaction at the core-mantle boundary (Ko et al., 2022). However, we argue that if this hypothesis is correct, carbon released from the core via plate tectonics is not strictly required. If a planet lacking plate tectonics shows an unusually high carbon content in its mantle, it could be because the iron carbide droplets encountered water molecules and then left carbon in its mantle during its core formation stage.
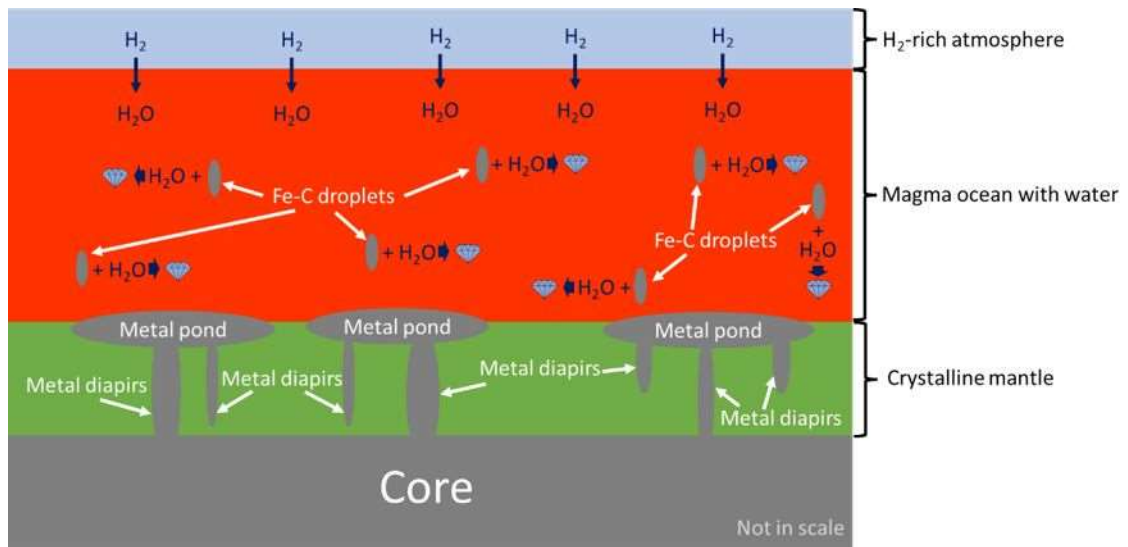

Figure 6. Illustration of iron carbide-water reaction in the early magma ocean. The hydrogen-rich atmosphere may have contributed water to the magma ocean (Young et al., 2023). The Fe-C alloy droplets eventually sink to the bottom of the magma ocean but would drift in the magma ocean for a period of time due to the convection. When Fe-C alloy encounters water, diamond forms and is left behind in the silicate portion of Earth.

Secondly, even if Fe-C alloy droplets were entirely drained to the core, metallic iron (Fe^0) is suggested to exist in the modern mantle below 250 km due to the $3\ Fe^{2+} = Fe^0 + 2\ Fe^{3+}$ disproportionation reaction (Armstrong et al., 2019; Bindi et al., 2020; Frost et al., 2004; Rohrbach et al., 2011; Rohrbach and Schmidt, 2011). When the Fe^0 encounters a carbon source such as carbonate or carbon hydrides, typically from organic sources on the subduction slabs, iron carbide forms (Kaminsky and Wirth, 2011; Lai et al., 2022). In fact, iron carbide in the modern mantle was also found as an inclusion in diamonds (Kaminsky and Wirth, 2011). If the water released by the slab, for example, dehydration from AlOOH (Piet et al., 2020) or phase H (Nishi et al., 2014), encounters this iron carbide, diamonds may also form, supporting the occurrence of iron carbide inclusions reported by Kaminsky and Wirth (2011). In addition to the water from the slab, the

mantle transition zone is potentially a significant water reservoir in the mantle, at least locally, and is observed to be hydrous (Karato, 2011; Koyama et al., 2013; Ohtani, 2020, 2015; Utada et al., 2009). Based on these studies, we consider that diamonds could also form when iron carbide on the slab encounters hydrous minerals in the transition zone. According to this scenario, diamonds could form anywhere below ~250 km, in locations such as those shown in Fig. 7, specifically:

1. The surface of the subduction slabs when the slab reaches the depth of iron carbide stable region diamond stable depth with low oxygen fugacity.

2. If the slab undergoes stagnation, the slab stays at the bottom of the transition zone for a period of time. Thus, bigger diamonds have sufficient time to grow.

3. When the slab keeps subducting, a diamond still forms at the surface of the slab. However, the production rate may be lower than that of Stage 1 and Stage 2 due to less water reaching such depth.

4. Core-water reaction may still release the diamond as Ko et al. 2022.
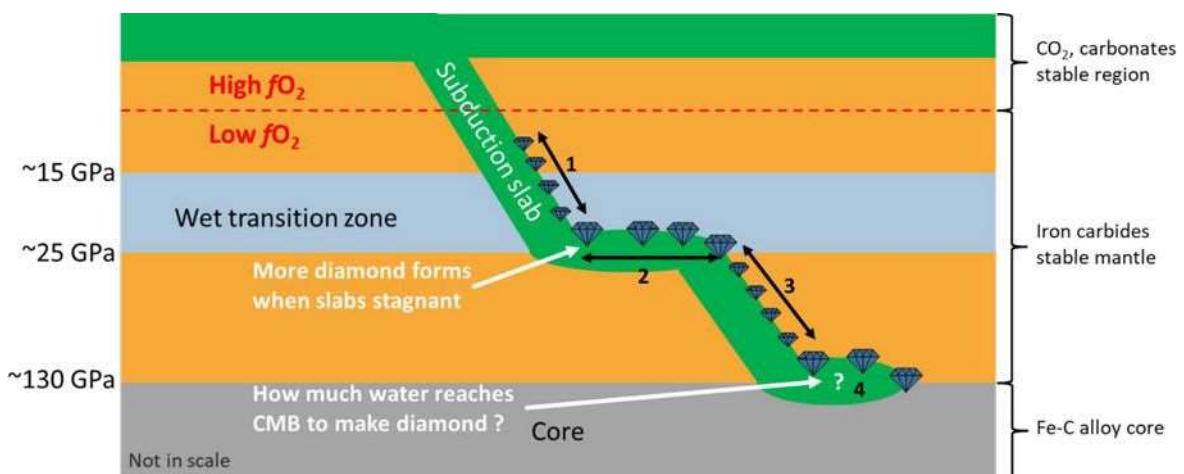

Figure 7. Illustration of specific places of diamond formation via iron carbide-water reaction in the modern mantle. The iron carbide-water reactions specifically occur at (1) the surface of the inclined slab, (2) the stagnant portion of the slab, (3) the surface of the inclined slab continues sinking to the core, and (4) the core-mantle boundary. The size of the diamond represents the general production rate of a diamond. A stagnated section of the plate and core-mantle boundary may generally have a greater abundance of diamonds due to the longer reaction period.

We cannot dismiss the possibility that the iron carbide-water reaction at the core-mantle boundary (Ko et al., 2022) is still taking place in the modern Earth and is a viable process for releasing carbon into the mantle. However, given that the iron carbide-water reaction can occur at

lower P-T conditions, a substantial amount of water might have been consumed by the iron carbide-water reaction on its way to the core-mantle boundary. Therefore, further investigation is required to determine the specific amount of water capable of reaching the core and releasing carbon into the silicate portion of Earth. If the water reaching the core-mantle boundary is revealed to be minor in future studies, an alternative model is necessary to explain the higher carbon concentration in the modern mantle.

References

Albarède, F., 2009. Volatile accretion history of the terrestrial planets and dynamic implications. Nature 461, 1227–1233. https://doi.org/10.1038/nature08477

Armstrong, K., Frost, D.J., McCammon, C.A., Rubie, D.C., Boffa Ballaran, T., 2019. Deep magma ocean formation set the oxidation state of Earth's mantle. Science 365, 903–906. https://doi.org/10.1126/science.aax8376

Bindi, L., Shim, S.-H., Sharp, T.G., Xie, X., 2020. Evidence for the charge disproportionation of iron in extraterrestrial bridgmanite. Sci. Adv. 6, eaay7893. https://doi.org/10.1126/sciadv.aay7893

Dalou, C., Hirschmann, M.M., Von Der Handt, A., Mosenfelder, J., Armstrong, L.S., 2017. Nitrogen and carbon fractionation during core–mantle differentiation at shallow depth. Earth and Planetary Science Letters 458, 141–151. https://doi.org/10.1016/j.epsl.2016.10.026

Dasgupta, R., Chi, H., Shimizu, N., Buono, A.S., Walker, D., 2013. Carbon solution and partitioning between metallic and silicate melt in a shallow magma ocean: Implications for the origin and distribution of terrestrial carbon. Geochimica et Cosmochimica Acta 102, 191–212. https://doi.org/10.1016/j.gca.2012.10.011

Deines, P., 2002. The carbon isotope geochemistry of mantle xenoliths. Earth-Science Reviews 58, 247–278. https://doi.org/10.1016/S0012-8252(02)00064-8

Dychalska, A., Popielarski, P., Franków, W., Fabisiak, K., Paprocki, K., Szybowicz, M., 2015. Study of CVD diamond layers with amorphous carbon admixture by Raman scattering spectroscopy. Materials Science-Poland 33, 799–805. https://doi.org/10.1515/msp-2015-0067

Fischer, R.A., Cottrell, E., Hauri, E., Lee, K.K.M., Le Voyer, M., 2020. The carbon content of Earth and its core. Proc. Natl. Acad. Sci. U.S.A. 117, 8743–8749. https://doi.org/10.1073/pnas.1919930117

Frost, D.J., Liebske, C., Langenhorst, F., McCammon, C.A., Trønnes, R.G., Rubie, D.C., 2004. Experimental evidence for the existence of iron-rich metal in the Earth's lower mantle. Nature 428, 409–412. https://doi.org/10.1038/nature02413

Glosli, J.N., Ree, F.H., 1999. Liquid-Liquid Phase Transformation in Carbon. Phys. Rev. Lett. 82, 4659–4662. https://doi.org/10.1103/PhysRevLett.82.4659

Grewal, D.S., Dasgupta, R., Sun, C., Tsuno, K., Costin, G., 2019. Delivery of carbon, nitrogen, and

sulfur to the silicate Earth by a giant impact. Sci. Adv. 5, eaau3669.
https://doi.org/10.1126/sciadv.aau3669

Guo, X., Yoshino, T., Chen, S., Wu, X., Zhang, J., 2022. Partial dehydration of brucite and its
implications for water distribution in the subducting oceanic slab. Geoscience Frontiers 13, 101342.
https://doi.org/10.1016/j.gsf.2021.101342

Hawkesworth, C.J., Cawood, P.A., Dhuime, B., 2020. The Evolution of the Continental Crust and
the Onset of Plate Tectonics. Front. Earth Sci. 8, 326. https://doi.org/10.3389/feart.2020.00326

Hirschmann, M.M., 2006. Water, Melting, and the Deep Earth H_2O Cycle. Annu. Rev. Earth Planet.
Sci. 34, 629–653. https://doi.org/10.1146/annurev.earth.34.031405.125211

Hirschmann, M.M., Dasgupta, R., 2009. The H/C ratios of Earth's near-surface and deep reservoirs,
and consequences for deep Earth volatile cycles. Chemical Geology 262, 4–16.
https://doi.org/10.1016/j.chemgeo.2009.02.008

Kaminsky, F., 2012. Mineralogy of the lower mantle: A review of 'super-deep' mineral inclusions in
diamond. Earth-Science Reviews 110, 127–147. https://doi.org/10.1016/j.earscirev.2011.10.005

Karato, S., 2011. Water distribution across the mantle transition zone and its implications for global
material circulation. Earth and Planetary Science Letters 301, 413–423.
https://doi.org/10.1016/j.epsl.2010.11.038

Kerridge, J.F., 1985. Carbon, hydrogen and nitrogen in carbonaceous chondrites: Abundances and
isotopic compositions in bulk samples. Geochimica et Cosmochimica Acta 49, 1707–1714.
https://doi.org/10.1016/0016-7037(85)90141-3

Knight, D.S., White, W.B., 1989. Characterization of diamond films by Raman spectroscopy. J.
Mater. Res. 4, 385–393. https://doi.org/10.1557/JMR.1989.0385

Ko, B., Chariton, S., Prakapenka, V., Chen, B., Garnero, E.J., Li, M., Shim, S., 2022. Water-Induced
Diamond Formation at Earth's Core-Mantle Boundary. Geophysical Research Letters 49,
e2022GL098271. https://doi.org/10.1029/2022GL098271

Koyama, T., Shimizu, H., Utada, H., Ichiki, M., Ohtani, E., Hae, R., 2013. Water Content in the
Mantle Transition Zone Beneath the North Pacific Derived from the Electrical Conductivity
Anomaly, in: Jacobsen, S.D., Van Der Lee, S. (Eds.), Geophysical Monograph Series. American
Geophysical Union, Washington, D. C., pp. 171–179. https://doi.org/10.1029/168GM13

Lai, X., Zhu, F., Gao, J., Greenberg, E., Prakapenka, V.B., Meng, Y., Chen, B., 2022. Melting of the
Fe-C-H System and Earth's Deep Carbon-Hydrogen Cycle. Geophysical Research Letters 49.
https://doi.org/10.1029/2022GL098919

Marty, B., 2012. The origins and concentrations of water, carbon, nitrogen and noble gases on
Earth. Earth and Planetary Science Letters 313–314, 56–66.
https://doi.org/10.1016/j.epsl.2011.10.040

McDonough, W.F., Sun, S. -s., 1995. The composition of the Earth. Chemical Geology, Chemical

Evolution of the Mantle 120, 223–253. https://doi.org/10.1016/0009-2541(94)00140-4

Ohtani, E., 2020. The role of water in Earth's mantle. National Science Review 7, 224–232. https://doi.org/10.1093/nsr/nwz071

Ohtani, E., 2015. Hydrous minerals and the storage of water in the deep mantle. Chemical Geology 418, 6–15. https://doi.org/10.1016/j.chemgeo.2015.05.005

Prawer, S., Nemanich, R.J., 2004. Raman Spectroscopy of Diamond and Doped Diamond. Philosophical Transactions: Mathematical, Physical and Engineering Sciences 362, 2537–2565.

Rohrbach, A., Ballhaus, C., Ulmer, P., Golla-Schindler, U., Schönbohm, D., 2011. Experimental Evidence for a Reduced Metal-saturated Upper Mantle. Journal of Petrology 52, 717–731. https://doi.org/10.1093/petrology/egq101

Rohrbach, A., Schmidt, M.W., 2011. Redox freezing and melting in the Earth's deep mantle resulting from carbon–iron redox coupling. Nature 472, 209–212. https://doi.org/10.1038/nature09899

Rubie, D.C., Nimmo, F., Melosh, H.J., 2015. Formation of the Earth's Core, in: Treatise on Geophysics. Elsevier, pp. 43–79. https://doi.org/10.1016/B978-0-444-53802-4.00154-8

Shi, L., Lu, W., Kagoshima, T., Sano, Y., Gao, Z., Du, Z., Liu, Y., Fei, Y., Li, Y., 2022. Nitrogen isotope evidence for Earth's heterogeneous accretion of volatiles. Nat Commun 13, 4769. https://doi.org/10.1038/s41467-022-32516-5

Utada, H., Koyama, T., Obayashi, M., Fukao, Y., 2009. A joint interpretation of electromagnetic and seismic tomography models suggests the mantle transition zone below Europe is dry. Earth and Planetary Science Letters 281, 249–257. https://doi.org/10.1016/j.epsl.2009.02.027

Wang, Z., Becker, H., 2013. Ratios of S, Se and Te in the silicate Earth require a volatile-rich late veneer. Nature 499, 328–331. https://doi.org/10.1038/nature12285

Wänke, H., 1981. Constitution of terrestrial planets. Phil. Trans. R. Soc. Lond. A.

Wood, B.J., Walter, M.J., Wade, J., 2006. Accretion of the Earth and segregation of its core. Nature 441, 825–833. https://doi.org/10.1038/nature04763

Young, E.D., Shahar, A., Schlichting, H.E., 2023. Earth shaped by primordial H_2 atmospheres. Nature 616, 306–311. https://doi.org/10.1038/s41586-023-05823-0